Observation of Giant Extrinsic Chirality Empowered by Quasi-Bound States in the Continuum

Jiaju Wu,[1] Xiaotian Xu,[1] Xiaoqiang Su,[2,†] Song Zhao,[3] Chao Wu,[3] Yong Sun,[1] Yunhui Li,[1] Feng Wu,[4,‡] Zhiwei Guo,[1,§] Haitao Jiang,[1,*] and Hong Chen[1]

[1] *Key Laboratory of Advanced Micro-Structured Materials, School of Physics Science and Engineering, Tongji University, Shanghai 200092, China*

[2] *Institute of Solid State Physics and College of Physics and Electronic Science, Shanxi Province Key Laboratory of Microstructure Electromagnetic Functional Materials, Shanxi Datong University, Datong 037009, China*

[3] *Shanghai Key Laboratory of Special Artificial Microstructure Materials and Technology, School of Physics Science and Engineering, Tongji University, Shanghai 200092, China*

[4] *School of Optoelectronic Engineering, Guangdong Polytechnic Normal University, Guangzhou 510665, China*

(Received 27 September 2021; revised 6 November 2021; accepted 18 November 2021; published 8 December 2021)

Without using intrinsic chiral metamaterials with complex structures, here we use achiral metasurfaces to realize giant extrinsic chirality empowered by quasi-bound states in the continuum (quasi-BICs). The giant extrinsic chirality in the proposed achiral metasurface is mainly attributed to the breaking of the mirror symmetry of the whole system, combining the metasurface with incident waves. The transmittance of two different polarization states and the signs of circular dichroism (CD) can be arbitrarily controlled by tilting the plane of the metasurface relative to the incoming waves. Remarkably, we simultaneously select two polarization states at different bands for a certain achiral metasurface based on the symmetry-protected dual bound states in the continuum (BICs). The measured maximum CDs approach ± 0.85. In addition, an application of the polarization-multiplexed-field image display assisted by chiral quasi-BICs is demonstrated. This work provides a general method to control extrinsic chirality in achiral metasurfaces and offers possibilities to design high-performance multiband spin-selective transmission, biodetection, chemical analysis, and on-chip chiral manipulation.

DOI: 10.1103/PhysRevApplied.16.064018

I. INTRODUCTION

Chirality, referring to a fundamental property in many systems that cannot be superimposed on their mirror images through rotational or translational transformation [1], has become a research hotspot, since it has significant applications, such as negative refraction [2–4], biodetection and chemical analysis [5–7], optical information processing [8], imaging [9–11], detector [12], and broadband wave plate [13]. Recently, the active tuning of a metamaterial [14] has been extended to dynamically tune the chiral properties of bilayered hybrid metamaterials [15]. However, the chiral interactions are very weak and hardly detectable in natural materials. Therefore, an enhancement of chirality is highly desirable. An increasing number of artificial chiral structures with intrinsic chirality have been proposed to achieve strong chiroptical effects, including chiral nanostructures [16,17], photonic crystals [18,19], fish-scale structures [20,21], reciprocal metamaterials [22], folded metamaterials [23], curled metasurfaces [24], origami-based metamaterials [25], and two-dimensional materials [26]. Nevertheless, chiroptical effects can be enhanced not only in chiral structures but also in achiral structures with extrinsic chirality [27]. Extrinsic chirality, i.e., achiral structures having mirror-symmetry planes together with an incident wave form a new system that cannot coincide with its mirror image, and thus, the whole system is chiral. This type of achiral structure, called an extrinsically chiral structure, has rapidly developed due to its promising simple structure design and manufacture [28–32] in comparison with the intrinsic chiral structures.

Recently, a kind of special localized mode lying inside continuous spectra, called the bound state in the continuum (BIC), has greatly attracted researchers' attention [33,34]. In 1929, von Neumann and Wigner predicted the existence of BICs in electronic systems [35]. Since then, BICs have been demonstrated in various systems [36–40]. There are two types of interesting BICs observed in photonics systems, including Friedrich-Wintgen BICs [41,42] and symmetry-protected BICs

*jiang-haitao@tongji.edu.cn
†suxqiang@outlook.com
‡fengwu@gpnu.edu.cn
§2014guozhiwei@tongji.e du.cn

 © 2021 American Physical Society

[43]. Friedrich-Wintgen BICs arise from the destructive interference between two radiating channels [38], while symmetry-protected BICs stem from the symmetry mismatch between localized modes and external propagating modes [33]. Although perfect BICs are very striking, they are unobservable from the spectrum, since they have vanishing spectral linewidths, i.e., infinite quality (Q) factors. In practice, by introducing external perturbations, perfect BICs would collapse to sharp Fano resonances with finite Q factors that are known as quasi-BICs with ultranarrow resonance linewidths, which can be utilized in various applications, such as lasers [44–46], acousto-optic modulators [47], nonlinear devices [48,49], wireless-power transfers [50], directional light emission [51], and sensors [52–54]. Therefore, an increasing variety of structures have been proposed to achieve quasi-BICs, including photonic waveguides [43], hybrid plasmonic-photonic structures [55,56], photonic crystal slabs [45,57–61], compound grating waveguide structures [62,63], asymmetric gratings [64–66], one-dimensional photonic crystals [67], anisotropic materials [68], and various metasurfaces [69–73]. Very recently, some fascinating metamaterials supporting quasi-BICs were proposed to efficiently control chirality. For example, Gorkunov *et al.* revealed that, by breaking the out-of-plane mirror symmetry, quasi-BICs can be achieved in intrinsic chiral metasurfaces [74]. Assisted by quasi-BICs with ultrahigh-Q factors, maximum intrinsic chirality can be achieved in the microwave regime [75]. Overvig *et al.* showed that a pair of twisted intrinsic chiral metasurfaces could support chiral quasi-BICs and efficiently control the chirality [76]. Kim and Kim revealed that, by breaking the in-plane inversion and mirror symmetries, high-Q chiroptical resonances by quasi-BICs in dielectric intrinsic chiral metasurfaces could be achieved [77]. These works open a door to explore chiral BICs in intrinsic chiral metasurfaces. Up to now, only quasi-BICs with intrinsic chirality have been observed; the possibility of extrinsic chirality governed by BICs remains unexplored. Therefore, can we utilize quasi-BICs to control the extrinsically chiral effect in achiral structure?

Compared to complex three-dimensional structures, the spatial configuration and symmetry of metasurfaces can be more flexibly designed and manufactured [78]. In this paper, we theoretically and experimentally demonstrate an achiral metasurface that possesses giant extrinsic chirality empowered by quasi-BICs and simultaneously supports two spin-selective transmission channels with reversing selectivity at oblique incidence. The strong extrinsic chirality arises from the combination of an achiral metasurface supporting BICs and oblique incident waves. We first transform BICs into quasi-BICs by breaking C_2 symmetry in the achiral metasurface. Then, we introduce chirality by breaking the out-of-plane mirror symmetry through tilting the plane of the metasurface relative to the incoming waves. Our design exhibits a sharp contrast in transmission between opposite circularly polarized light, which is referred to as left circularly polarized (LCP) light and right circularly polarized (RCP) light. The maximum of measured circular dichroism (CD) is close to ± 0.85. The maximal transmittance is more than 0.87 of the chosen circularly polarized light, while its counterpart is close to zero. Moreover, the extrinsic chirality can be efficiently controlled by the tilted angle and in the opposite direction yields the opposite sign in the CD spectrum. Most strikingly, we also achieve double transmission channels with opposite spin-selective properties based on dual quasi-BICs at the same tilted angle. Finally, as an example of application, the polarization-multiplexed-field image display assisted by chiral quasi-BICs is demonstrated. This type of achiral metasurface may provide an avenue to design various chiral devices, including circularly polarized spectral filters, spin-selective wavelength multiplexers, and ultrasensitive biomolecular sensors.

II. MODEL AND METHOD

The schematic of the proposed achiral metasurface is shown in Fig. 1(a). The achiral metasurface consists of an array of metal subwavelength double-gap split-ring resonators (DSRRs) supported by a commercial printed substrate F4BM, which is a kind of Teflon copper-clad laminates ($\varepsilon_r = 2.2$, $\tan\delta = 0.009$), with a thickness of $h = 1.6$ mm, as illustrated in Fig. 1(b). Here, the material of the DSRRs is selected to be Cu. The geometric parameters of the DSRRs are selected as follows: the length of the square resonator is $l = 20$ mm, the width is $w = 2.15$ mm, the gap size is $g = 1$ mm, and the thickness is $t = 0.035$ mm. The period of the unit cell is $\Lambda = 22.2$ mm. The structure sample is approximately 1500×1800 mm^2 and the size of the unit cell is smaller than the wavelength, which indicates that diffraction can be neglected at the normal or oblique incidence [28]. We now consider an original subwavelength DSRR together with the incident wave vector, as shown in Fig. 1(c). The structure is symmetric with respect to three types of mirror planes, namely, σ_1, σ_2, and out of the plane. The original metasurface possesses neither intrinsic nor extrinsic chirality at normal incidence, since its C_2 rotational symmetry and out-of-plane mirror symmetry are not broken. The structure cannot distinguish the two spin states of light (i.e., LCP and RCP light). In other words, the transmittance spectra of the structure are identical for LCP and RCP incident light. To obtain giant extrinsic chirality and obviously break the spin degeneracy in the spectra, one can simultaneously introduce two parameters, δ (i.e., displacing one gap from the center by a distance) and tilted angle θ (i.e., tilting the structure around the y axis), to establish a chiral system that breaks all mirror symmetries, as illustrated in Fig. 1(d).

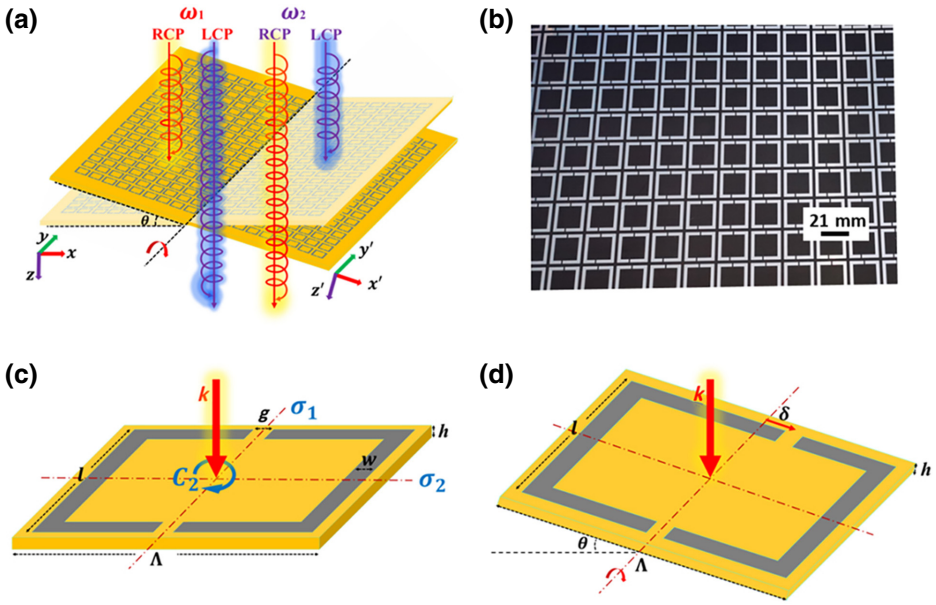

FIG. 1. (a) Schematic of the proposed achiral metasurface. ω_1 and ω_2 represent different operating frequencies. Functionality of the proposed structure is to transmit the designated circularly polarized wave while blocking its counterpart at the multiband. (b) Photograph of the fabricated sample. (c) Schematic representation of a unit cell of the metasurface, which possesses C_2 rotational symmetry and out-of-plane mirror symmetry. (d) Schematic representation of a unit cell of the metasurface, which does not possess C_2 rotational symmetry and out-of-plane mirror symmetry. δ and θ represent the offset and tilted angles, respectively.

We consider $e^{-i\omega t}$, the time dependence of waves propagating in the positive z direction. The wave polarized along complex unit vectors can be expressed in

$$\mathbf{e}_{\pm} = (\mathbf{e}_x \mp \mathbf{e}_y)/\sqrt{2}. \tag{1}$$

Here, $\mathbf{e}_+$ and $\mathbf{e}_-$ correspond to RCP and LCP, respectively. Generally, this type of transmission-reflection problem can be described by the S-matrix equation. The key optical parameters of chirality are CD $\mathcal{C}$ and optical rotation (OR) $\mathcal{O}$ [29,74]:

$$\mathcal{C} = |t_R|^2 - |t_L|^2 \text{ and } \mathcal{O} = \arg t_R - \arg t_L, \tag{2}$$

where t_R and t_L are the transmission coefficients of RCP and LCP light, respectively; $\arg t_R$ and $\arg t_L$ correspond to the transmission phases of RCP and LCP light, respectively. To obtain giant extrinsic chirality, the spin degeneracy need be broken. In the following, we reveal a step-by-step design to break the spin degeneracy by transforming BICs into quasi-BICs and achieve chirality manipulation in the achiral metasurface with different tilted angles.

How a true BIC is transformed into a quasi-BIC via breaking the symmetry of the periodic structure has been studied in detail [68–71]. Although dual quasi-BICs are observed in an achiral metasurface by breaking C_2 symmetry at different resonance frequencies, they basically stem from a similar mechanism. No matter whether it is a lower or higher resonance frequency, the quasi-BICs are formed due to the emergence of two pairs of antiresonance electric dipoles. Without loss of generality, we now shown the higher-frequency branch. The unit cell possesses C_2 symmetry and out-of-plane mirror symmetry, and the electric resonance of this symmetry is described by two pairs of dipole moments ($\mathbf{P}_1$, $\mathbf{P}_2$ and $\mathbf{P}_3$, $\mathbf{P}_4$) shown in the plane of the drawings in Fig. 2. To estimate the two distinct spin states of light coupling with the incident wave polarized along with the unit vector $\mathbf{e}$ and possessing wave vector $\mathbf{k}$ along the positive z axis, one can integrate the incident-wave field with its current density [69,74]:

$$m_{\mathbf{e}} \propto \int_{V_1,\ V_2} d\mathbf{r}[\mathbf{j}(\mathbf{r}) \cdot \mathbf{e}] e^{i\mathbf{k}(\mathbf{r}\cdot\mathbf{e}_{x'})\sin\theta}, \tag{3}$$

where $m_{\mathbf{e}}$ is the parameter describing the coupling of two spin states; V_1 and V_2 are the volumes of two branches of DSRR, respectively. $\mathbf{e}_{x'}$ is the unit vector after tuning the tilted angle, θ, of the plane of the metasurface relative to the y axis, which can be obtained by coordinate transformation. For each volume, the integral yields the dipole moment of the corresponding branch. For all incident-wave polarizations, the sum of the dipole moment of each volume is zero due to symmetry protection, which can be described as $m_{\mathbf{e}} \propto \sum_i \mathbf{P}_i \cdot \mathbf{e} = 0$. As a proof of concept, a schematic illustration of the dipole moments for the RCP wave is shown in Fig. 2(a). The distribution of the dipole moments for the LCP wave is similar, so we just show the RCP wave. One can see that the dipole moments cancel each other out, which means symmetry-protected BICs occur for all normally incident waves.

The true BICs would become quasi-BICs by introducing external perturbations, δ, to break the C_2 rotational symmetry. One can obtain the parameters of coupling to different circularly polarized waves from Eq. (3), which can be described as $m_{\mathbf{e}} \propto \sum_i \mathbf{P}_i \cdot \mathbf{e} \neq 0$. Although external perturbations, δ, break the C_2 rotational symmetry (i.e., eliminating mirror planes σ_1 and σ_2), the out-of-plane mirror symmetry remains, as shown in Fig. 2(b); therefore, they are achiral at normal incidence. Another way to break the symmetry is to introduce the oblique incidence, which

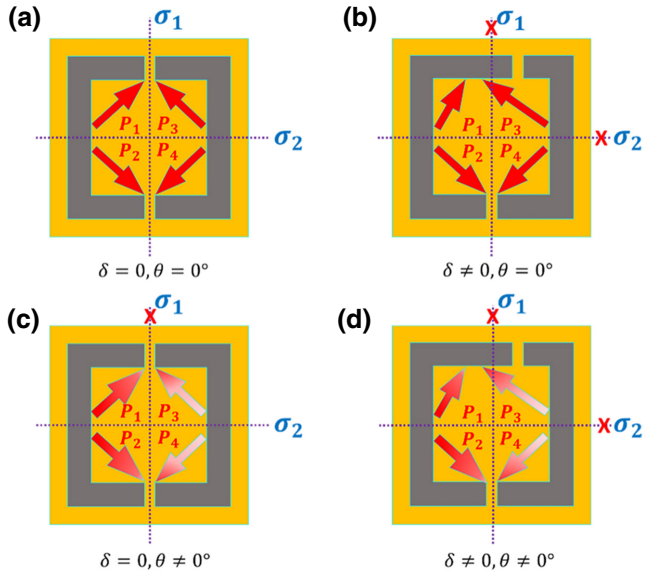

FIG. 2. (a) Electric-dipole-moment distribution of BICs at $\delta = 0$ and $\theta = 0°$. Unit cell possesses C_2 symmetry (i.e., mirror planes are σ_1 and σ_2) and out-of-plane mirror symmetry. (b) Electric-dipole-moment distribution of quasi-BICs at $\delta \neq 0$ and $\theta = 0°$. (c) Electric-dipole-moment distribution of quasi-BICs at $\delta = 0$ and $\theta \neq 0°$. (d) Electric-dipole-moment distribution of chiral quasi-BICs at $\delta \neq 0$ and $\theta \neq 0°$.

TABLE I. Summary of extrinsic chirality assisted by quasi-BICs in an achiral metasurface.

δ	θ	σ_1	σ_2	Out of plane	Quasi-BICs	Chirality
Zero	Zero	✓	✓	✓	No	No
Nonzero	Zero	×	×	✓	Yes	No
Zero	Nonzero	×	✓	×	Yes	No
Nonzero	Nonzero	×	×	×	Yes	Yes

can break out-of-plane mirror symmetry together with mirror plane σ_1 when the external offset is $\delta = 0$, the corresponding coupling parameters $m_\pm$ are equal but nonzero at incident light with inverse polarization rotations. They are also achiral because the structure retains mirror plane σ_2, as shown in Fig. 2(c). One can simultaneously combine offset δ with incident angle θ to break all mirror symmetries, including in-plane and out-of-plane symmetries, as illustrated in Fig. 2(d). Therefore, the whole system is composed of an achiral metasurface and the obliquely incident wave is chiral, which ensures the rise of optical chirality: $m_+ \neq m_- \neq 0$ [74].

In summary, the following key routes for designing chirality in achiral metasurface are identified, as shown in Table I. One can see that, if any symmetry plane is broken, BICs become quasi-BICs, but they are achiral due to the partial symmetry plane still being preserved. If all symmetry planes are destroyed, the whole system composed of the achiral metasurface and the obliquely incident wave is chiral.

III. RESULT AND DISCUSSION

To prove the above theoretical analysis, we conduct full-wave simulations, which are performed using CST Microwave Studio using a finite-element frequency-domain solver with unit-cell boundary conditions in the x

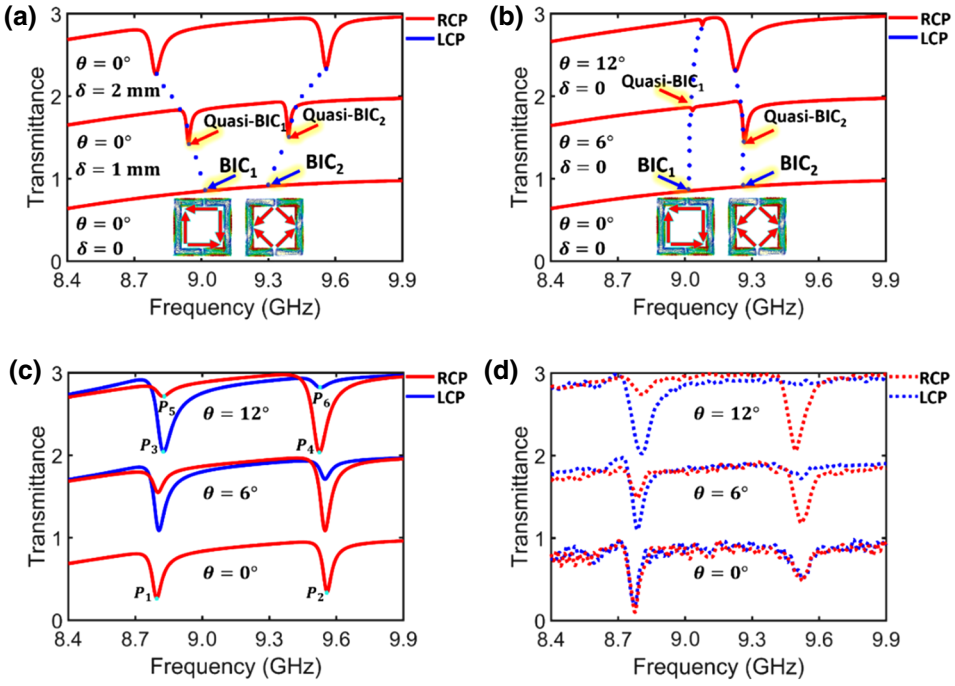

FIG. 3. Dependence of transmittance spectra of the structure on (a) offset δ and (b) tilted angle θ. Insets represent distributions of surface current and dipole moments within the structure, corresponding to dual BICs. (c) Simulated transmittance spectra of two distinct spin states for different θ at $\delta = 2$ mm. (d) Corresponding measured transmittance spectra. Red and blue lines represent RCP and LCP waves, respectively.

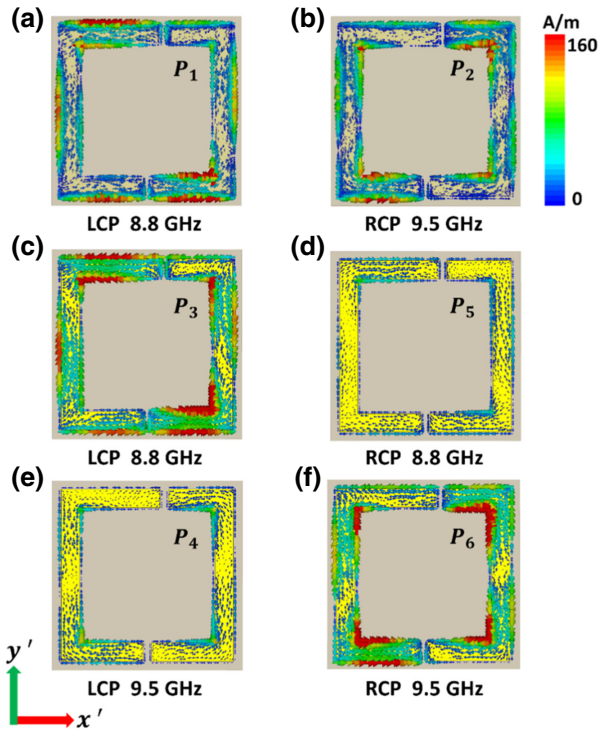

FIG. 4. Simulated surface-current distributions for (a) lower-frequency and (b) higher-frequency branches within metasurfaces without chiral response under LCP or RCP wave incidences. Surface-current distributions for (c),(d) lower-frequency and (e),(f) higher-frequency branches within the metasurface with chiral responses under (c),(e) LCP and (d),(f) RCP incoming waves.

and y directions and Floquet ports in the z direction. On the other hand, the experimental measurements are performed in an anechoic chamber using microwave broadband horn antennas equipped with a vector-network analyzer (Agilent PNA network analyzer N5222A). To illustrate chirality in the metasurface presented above, we first simulate the transmittance of the achiral metasurface at normal incidence as offset δ changes from 0 to 2 mm, and the transmittance as incidence angle θ changes from 0° to 12° at offset $\delta = 0$, as shown in Figs. 3(a) and 3(b), respectively. It is seen that the transmittance spectra exhibit dual asymmetric Fano line shapes, which originate from external perturbations δ or θ; this breaks the symmetry of the structure. The bound states leaking (coupling) to the propagating modes give rise to the formation of dual quasi-BICs. As δ or θ gradually increases, the bandwidth of the transmittance spectra is reduced noticeably, since the coupling between two antiresonance electric dipoles and the incoming radiation becomes weak. Notably, transmittance spectra are slightly different due to the different ways of the symmetry breaking. The line shapes and positions of the corresponding quasi-BICs depend weakly on tilted angle θ. Compared to Fig. 3(a), the transmittance spectra of the achiral metasurface in Fig. 3(b) exhibit a weaker resonance feature, which is mainly caused by the loss of the substrate F4BM. Although the symmetry of the structure is broken in two different pathways, the dual-symmetry-protected BICs are the same type, which is determined by the structure itself. As proof, in two cases, the surface-current distributions and dipole moments for the lower- and higher-frequency branches of BICs are shown in the insets. One can see that the surface-current distributions and dipole moments are identical for the lower and higher frequency branches of BICs, respectively. The transmittance spectra of the structure are identical for LCP and RCP incident light since symmetry planes are not completely broken, which implies that there is no chirality.

By contrast, if we tune offset δ and tilted angle θ simultaneously, both of the symmetry planes can be broken simultaneously, leading to the chiral responses, which provides transmission of one spin state of incident waves while blocks its counterpart. We further study the dependence of the transmittance on tilted angle θ when offset δ is chosen to be 2 mm, as shown in Fig. 3(c). At normal incidence, the transmittance spectra of the structure are identical for LCP and RCP waves. As the tilted angle of the structure relative to the incoming wave increases, the spin degeneracy is broken gradually. In other words, significant difference in transmittance spectra between LCP and RCP waves occurs. It can be observed that the transmittance of LCP wave greatly increases at the higher frequency branch as the tilted angle θ increases while that of RCP wave gradually decreases. When $\theta = 12°$, the simulated transmittance of LCP wave reaches 0.87 at the resonance frequency of 9.5 GHz while the transmittance of RCP wave is dramatically suppressed (i.e., near zero). Interestingly, the situation is reversed at the lower frequency branch, in which the quasi-BICs of achiral metasurface reverse its chirality. The transmittance spectra of achiral metasurface exhibit a strong resonance feature with a minimum transmittance of 0.02 at 8.8 GHz for LCP wave while maintains high-efficiency transmission up to 0.85 for RCP wave. Figure 3(d) shows the experimentally measured transmittance spectra corresponding to Fig. 3(c). The experimental results agree well with numerical simulations. The huge discrepancy between the two distinct spin states of light of transmitted light manifests strong extrinsic chiral responses in achiral metasurface.

Physically, the interaction between the achiral metasurface and LCP (RCP) wave can be further validated by the surface current within the structure. Therefore, to further understand the distinct extrinsic chiral responses at the multiband in achiral metasurfaces, the surface-current distributions at different resonant frequencies are plotted and compared for two distinct spin states of light, as shown in Fig. 4. In the case of $\delta = 2$ mm and $\theta = 0°$, the achiral metasurface strongly couples with RCP and

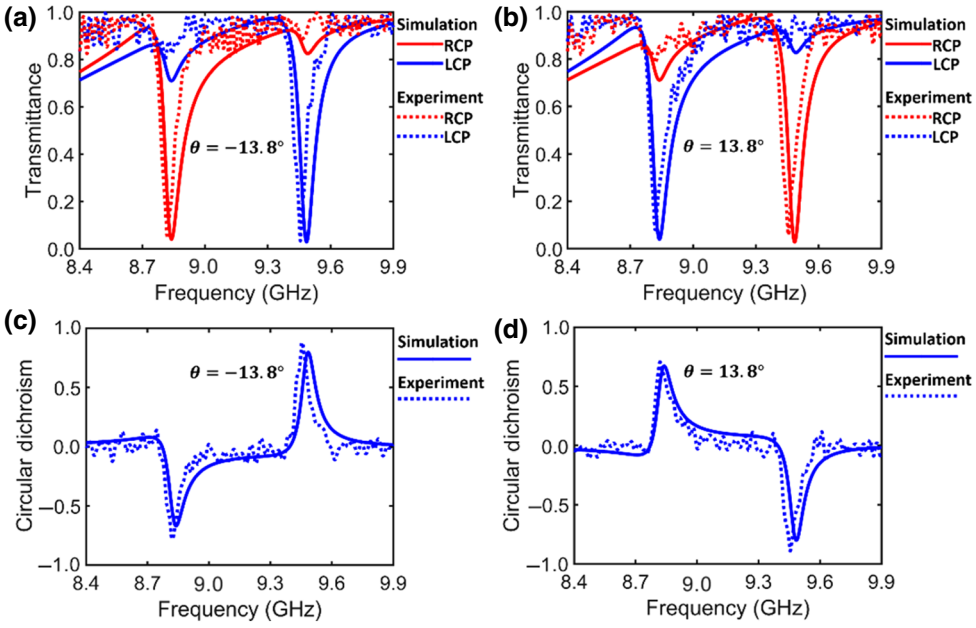

FIG. 5. Transmittance spectra of the structure for RCP (red solid line) and LCP (blue solid line) waves at (a) $\theta = -13.8^\circ$ and (b) $\theta = 13.8^\circ$. (c),(d) Corresponding CD spectra. Solid and dashed lines represent simulated and experimental results, respectively.

LCP waves and exhibits a double-resonance feature with a transmittance minimum [corresponding to Fig. 3(c)]. For the lower- and higher-frequency resonances appearing at around 8.8 and 9.5 GHz, the corresponding surface currents excited in the achiral metasurface are shown in Figs. 4(a) and 4(b), respectively. Since the out-of-plane mirror symmetry remains [see Fig. 2(b)], no chiral response occurs at normal incidence. In the second case of $\delta = 2$ mm and $\theta = 12^\circ$, the achiral metasurface uncouples with LCP light and is resonantly coupled to its counterpart at around 9.5 GHz, while the situation is reversed at the lower-frequency branch [see Fig. 3(c)], corresponding to different chirality behavior. For the lower-frequency branch, the interaction between the achiral metasurface and LCP wave is much stronger than that of its counterpart, since the surface current on the surface of the structures is significantly enhanced, as shown in Figs. 4(c) and 4(d). Compared with the lower-frequency branch, the interaction between the achiral metasurface and the LCP wave is weaker than that of its counterpart because the current on the surface of the structures is highly suppressed, as illustrated in Figs. 4(e) and 4(f). As a result, different coupling between the achiral metasurface and LCP (RCP) wave yields completely reversed extrinsic chirality at different frequencies.

To reveal strong extrinsic chiral responses and dual-channel spin-selective transmission, the simulated and experimental transmittance spectra of the metasurface at $\theta = \pm 13.8^\circ$ are plotted in Figs. 5(a) and 5(b), respectively. One can see the spin-selective transmission at different bands and the situation is reversed with the opposite incidence angle. The extrinsic chirality of the metasurface can be quantitatively characterized according to Eq. (2). Figures 5(c) and 5(d) show the theoretical and experimental CD spectra of the structure for equally tilted angles in opposite directions ($\theta = -13.8^\circ$ and $\theta = 13.8^\circ$), respectively. Two reversed resonances occur in the CD spectra, which clearly illustrate that the metasurface exhibits distinct chirality responses at the multiband. Figure 5(c) shows the theoretical and experimental CD spectra of the metasurface reaching up to the maximum values of 0.8 and 0.85 at the higher-frequency branch, respectively, while there are two small CD peaks as low as -0.72 and -0.81 at the lower-frequency branch, indicating very strong extrinsic chirality [28,29,32]. It is worth noting that the CD spectra for RCP and LCP waves reverse when the angle is tilted in the opposite direction, as shown in Fig. 5(d). In comparison with the simulated transmittance spectra, the measured result appears to be slightly shifted due to the imperfection of the structure and the finite size of the structure. Nevertheless, this small deviation will not affect the result. The experimental results still agree well with the theoretical simulations, which prove the validity of the model. So far, we both theoretically and experimentally demonstrate another avenue to design giant extrinsic chirality and multispectral spin-selective transmission assisted by quasi-BICs in achiral structures.

Finally, to better show the giant extrinsic chirality empowered by quasi-BICs in an achiral metasurface, we use two enantiomers to create a pattern containing one letter "T" and simulate the field distributions under LCP and RCP wave incidences, respectively. Figure 6(a) shows the configuration of the pattern, where the letter T is denoted by A and the rest is denoted by B. The pattern array is composed of 30×40 unit cells. Parts A and B possess different chiral responses for LCP or RCP waves. Without loss of generality, we choose one chiral BIC at 9.5 GHz from Fig. 5(b) as the operating frequency. Figures

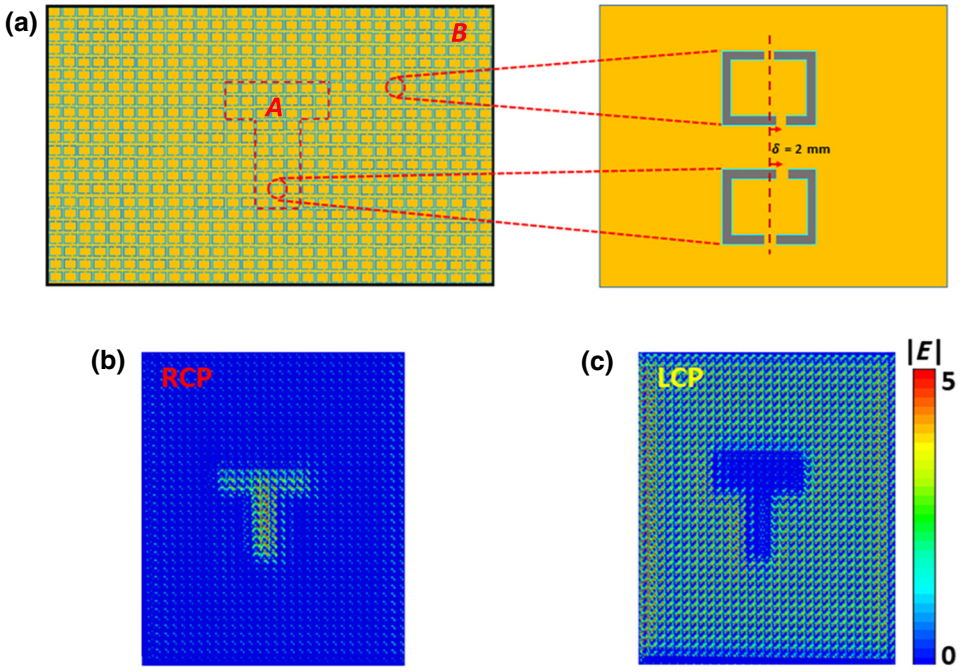

FIG. 6. (a) Schematic of the pattern containing letter T. Insets show the unit cells in part *A* and part *B*. (b), (c) Simulated electric field distributions on the metasurface under RCP and LCP wave illuminations, respectively.

6(b) and 6(c) show the simulated electric field distributions on the metasurface under the RCP and LCP wave illuminations, respectively. One can see that, under the RCP wave incidence, as shown in Fig. 6(b), the electric field in the letter T letter part is strong because of the resonant coupling between part *A* and the RCP wave around 9.5 GHz [corresponding to the frequency of one chiral BIC in Fig. 5(b)], while the electric field in background part *B* is weak because the chirality is very weak. For the LCP wave illumination, the situation is reversed. The electric field in the letter T part is weak, while that in background part *B* is strong, as shown in Fig. 6(c). Therefore, the field-image display can be flexibly tuned by changing the polarization of the incidence waves. The switching between "*on*" and "*off* " states for RCP or LCP wave incidence can be realized. This means that chiral quasi-BICs can be utilized in the application of the polarization-multiplexed-field image display.

IV. CONCLUSIONS

Herein, an achiral metasurface possessing giant extrinsic chirality empowered by quasi-BICs is theoretically and experimentally investigated, when the mirror symmetry of the whole system, combining the achiral metasurface with incident waves, is broken. The experimental results agree well with theoretical simulations, which prove the validity of the model. Although our results are based on the microwave regime, the concept of extrinsic chirality assisted by quasi-BICs can be extended to a higher-frequency range. Moreover, the transmittance of two distinct spin states at the multiband, and the signs of CD can be flexibly adjusted by tilting the plane of the metasurface relative to the incident waves. As an example of an application, the polarization-multiplexed-field image display assisted by quasi-BICs is also given. Our work provides a straightforward strategy to realize giant extrinsic chirality and has great potential applications in multiband spin-selective transmission, biodetection, chemical analysis, and on-chip chiral manipulation.

ACKNOWLEDGMENTS

This work is sponsored by the National Key Research Program of China (Grant No. 2016YFA0301101), the National Natural Science Foundation of China (Grants No. 11774261, No. 61621001, No. 91850206, No. 12004284, No. 11974261, No. 11874286, No. 11774057, and No. 12104105), the Fundamental Research Funds for the Central Universities (Grant No. 22120190222), the Shanghai Super Postdoctoral Incentive Program (Grant No. 2019TQ0232), the China Postdoctoral Science Foundation (Grant No. 2019M661605), and the Start-up Funding of Guangdong Polytechnic Normal University (Grant No. 2021SDKYA033). We deeply thank Dr. Li He, Mr. Caifu Fan, and Mr. Yueyang Min for their help with experiments and discussions.

[1] W. Kelvin, *The Molecular Tactics of a Crystal* (Clarendon Press, UK, 1894).
[2] J. B. Pendry, A chiral route to negative refraction, Science **306**, 1353 (2004).

[3] S. Zhang, Y. S. Park, J. Li, X. Lu, W. Zhang, and X. Zhang, Negative Refractive Index in Chiral Metamaterials, Phys. Rev. Lett. **102**, 023901 (2009).

[4] E. Plum, J. Zhou, J. Dong, V. A. Fedotov, T. Koschny, C. M. Soukoulis, and N. I. Zheludev, Metamaterial with negative index due to chirality, Phys. Rev. B **79**, 035407 (2009).

[5] E. Hendry, T. Carpy, J. Johnston, M. Popland, R. V. Mikhaylovskiy, A. J. Lapthorn, S. M. Kelly, L. D. Barron, N. Gadegaard, and M. Kadodwala, Ultrasensitive detection and characterization of biomolecules using superchiral fields, Nat. Nanotech. **5**, 783 (2010).

[6] Y. Zhao, A. N. Askarpour, L. Sun, J. Shi, X. Li, and A. Alù, Chirality detection of enantiomers using twisted optical metamaterials, Nat. Commun. **8**, 14180 (2017).

[7] G. Palermo, G. E. Lio, M. Esposito, L. Ricciardi, M. Manoccio, V. Tasco, A. Passaseo, A. D. Luca, and G. Strangi, Biomolecular sensing at the interface between chiral metasurfacesand hyperbolic metamaterials, ACS Appl. Mater. Interfaces **12**, 30181 (2020).

[8] Y. Chen, X. Yang, and J. Gao, 3D janus plasmonic helical nanoapertures for polarization-encrypted data storage, Light Sci. Appl. **8**, 45 (2019).

[9] Y. Chen, X. Yang, and J. Gao, Spin-controlled wavefront shaping with plasmonic chiral geometric metasurfaces, Light Sci. Appl. **7**, 84 (2018).

[10] G. Zheng, H. Mühlenbernd, M. Kenney, G. Li, T. Zentgraf, and S. Zhang, Metasurface holograms reaching 80% efficiency, Nat. Nanotech. **10**, 308 (2015).

[11] Q. Wang, E. Plum, Q. Yang, X. Zhang, Q. Xu, Y. Xu, J. Han, and W. Zhang, Reflective chiral meta-holography: Multiplexing holograms for circularly polarized waves, Light Sci. Appl. **7**, 25 (2008).

[12] W. Li, Z. J. Coppens, L. V. Besteiro, W. Wang, A. O. Govorov, and J. Valentine, Circularly polarized light detection with hot electrons in chiral plasmonic metamaterials, Nat. Commun. **6**, 8379 (2015).

[13] C. Wu, H. Li, X. Yu, F. Li, H. Chen, and C. T. Chan, Metallic Helix Array as a Broadband Wave Plate, Phys. Rev. Lett. **107**, 177401 (2011).

[14] Y. Xiang, X. Dai, J. Guo, H. Zhang, S. Wen, and D. Tang, Critical coupling with graphene-based hyperbolic metamaterials, Sci. Rep. **4**, 5483 (2014).

[15] T. T. Lv, Y. X. Li, H. F. Ma, Z. Zhu, Z. P. Li, C. Y. Guan, J. H. Shi, H. Zhang, and T. J. Cui, Hybrid metamaterial switching for manipulating chirality based on VO_2 phase transition, Sci. Rep. **6**, 23186 (2016).

[16] J. K. Gansel, M. Thiel, M. S. Rill, M. Decker, K. Bade, V. Saile, G. von Freymann, S. Linden, and M. Wegener, Gold helix photonic metamaterial as broadband circular polarizer, Science **325**, 1513 (2009).

[17] M. Schäferling, D. Dregely, M. Hentschel, and H. Giessen, Tailoring Enhanced Optical Chirality: Design Principles for Chiral Plasmonic Nanostructures, Phys. Rev. X **2**, 031010 (2012).

[18] M. Thiel, G. von Freymann, and M. Wegener, Layer-by-layer three-dimensional chiral photonic crystals, Opt. Lett. **32**, 2547 (2007).

[19] F. Li, X. Huang, J. Lu, J. Ma, and Z. Liu, Weyl points and Fermi arcs in a chiral phononic crystal, Nat. Phys. **14**, 30 (2018).

[20] V. A. Fedotov, P. L. Mladyonov, S. L. Prosvirnin, A. V. Rogacheva, Y. Chen, and N. I. Zheludev, Asymmetric Propagation of Electromagnetic Waves Through a Planar Chiral Structure, Phys. Rev. Lett. **97**, 167401 (2006).

[21] S. Yoo and Q. Park, Chiral Light-Matter Interaction in Optical Resonators, Phys. Rev. Lett. **114**, 203003 (2015).

[22] M. Xiao, Q. Lin, and S. Fan, Hyperbolic Weyl Point in Reciprocal Chiral Metamaterials, Phys. Rev. Lett. **117**, 057401 (2016).

[23] S. Yang, Z. Liu, H. Yang, A. Jin, S. Zhang, J. Li, and C. Gu, Intrinsic chirality and multispectral spin-selective transmission in folded Eta-shaped metamaterials, Adv. Opt. Mater. **8**, 1901448 (2020).

[24] C. Wang, Z. Li, R. Pan, W. Liu, H. Cheng, J. Li, W. Zhou, J. Tian, and S. Chen, Giant intrinsic chirality in curled metasurfaces, ACS Photonics **7**, 3415 (2020).

[25] Z. Wang, L. Jing, K. Yao, Y. Yang, B. Zheng, C. M. Soukoulis, H. Chen, and Y. Liu, Origami-Based reconfigurable metamaterials for tunable chirality, Adv. Opt. Mater. **29**, 1700412 (2017).

[26] Q. Hong, W. Xu, J. Zhang, Z. Zhu, X. Yuan, and S. Qin, Optical activity in monolayer black phosphorus due to extrinsic chirality, Opt. Lett. **44**, 1774 (2019).

[27] R. Williams, Optical Rotatory Effect in the Nematic Liquid Phase of p-Azoxyanisole, Phys. Rev. Lett. **21**, 342 (1968).

[28] E. Plum, V. A. Fedotov, and N. I. Zheludev, Optical activity in extrinsically chiral metamaterial, Appl. Phys. Lett. **93**, 191911 (2008).

[29] E. Plum, X. X. Liu, V. A. Fedotov, Y. Chen, D. P. Tsai, and N. I. Zheludev, Metamaterials: Optical Activity Without Chirality, Phys. Rev. Lett. **102**, 113902 (2009).

[30] J. H. Shi, Q. C. Shi, Y. X. Li, G. Y. Nie, C. Y. Guan, and T. J. Cui, Dual-polarity metamaterial circular polarizer based on giant extrinsic chirality, Sci. Rep. **5**, 16666 (2015).

[31] L. Mao, K. Liu, S. Zhang, and T. Cao, Extrinsically 2D-chiral metamirror in near-infrared region, ACS Photonics **7**, 375 (2020).

[32] S. Yang, Y. Li, X. Chen, Q. Yang, J. Han, and W. Zhang, Extrinsic optical activity in all-dielectric terahertz metamaterial, Opt. Lett. **22**, 6146 (2020).

[33] C. W. Hsu, B. Zhen, A. D. Stone, J. D. Joannopoulos, and M. Soljačić, Bound state in the continuum, Nat. Rev. Mater. **1**, 16048 (2016).

[34] A. F. Sadreev, Interference traps waves in an open system: Bound states in the continuum, Rep. Prog. Phys. **84**, 055901 (2021).

[35] J. von Neumann and E. P. Wigner, Über merkwürdige diskrete eigenwerte, Phys. Z. **30**, 465 (1929).

[36] H. Friedrich and D. Wintgen, Interfering resonances and bound states in the continuum, Phys. Rev. A **32**, 3231 (1985).

[37] C. M. Linton and P. McIver, Embedded trapped modes in water waves and acoustics, Wave Motion **45**, 16 (2007).

[38] H. Krüger, On the existence of embedded eigenvalues, J. Math. Anal. Appl. **395**, 776 (2012).

[39] D. C. Marinica, A. G. Borisov, and S. V. Shabanov, Bound States in the Continuum in Photonics, Phys. Rev. Lett. **100**, 183902 (2008).

[40] W. Liu, B. Wang, Y. Zhang, J. Wang, M. Zhao, F. Guan, X. Liu, L. Shi, and J. Zi, Circularly polarized states spawning

from bound states in the continuum, Phys. Rev Lett. **123**, 116104 (2019).
[41] S. G. Tikhodeev, A. L. Yablonskii, E. A. Muljarov, N. A. Gippius, and T. Ishihara, Quasiguided modes and optical properties of photonic crystal slabs, Phys. Rev. B **66**, 045102 (2002).
[42] A. Christ, S. G. Tikhodeev, N. A. Gippius, J. Kuhl, and H. Giessen, Waveguide-plasmon Polaritons: Strong Coupling of Photonic and Electronic Resonances in a Metallic Photonic Crystal Slab, Phys. Rev. Lett. **91**, 183901 (2003).
[43] E. N. Bulgakov and A. F. Sadreev, Bound states in the continuum in photonic waveguides inspired by defects, Phys. Rev. B **79**, 075105 (2008).
[44] K. Hirose, Y. Liang, Y. Kurosaka, A. Watanabe, T. Sugiyama, and S. Noda, Watt-class high-power, highbeam-quality photonic-crystal lasers, Nat. Photonics **8**, 406 (2014).
[45] A. Kodigala, T. Lepetit, Q. Gu, B. Bahari, Y. Fainman, and B. Kanté, Lasing action from photonic bound states in continuum, Nature **541**, 196 (2017).
[46] Q. Song, J. Hu, S. Dai, C. Zheng, D. Han, J. Zi, Z. Q. Zhang, and C. T. Chan, Coexistence of a new type of bound state in the continuum and a lasing threshold mode induced by PT symmetry, Sci. Adv. **6**, 1160 (2020).
[47] Z. Yu and X. Sun, Acousto-optic modulation of photonic bound state in the continuum, Light Sci. Appl. **9**, 1 (2020).
[48] M. I. Molina, A. E. Miroshnichenko, and Y. S. Kivshar, Surface Bound States in the Continuum, Phys. Rev. Lett. **108**, 070401 (2012).
[49] Z. Liu, Y. Xu, Y. Lin, J. Xiang, T. Feng, Q. Cao, J. Li, S. Lan, and J. Liu, High-Q Quasibound States in the Continuum for Nonlinear Metasurfaces, Phys. Rev. Lett. **123**, 253901 (2019).
[50] Y. Xie, Z. Zhang, Y. Lin, T. Feng, and Y. Xu, Magnetic Quasi-Bound State in the Continuum for Wireless Power Transfer, Phys. Rev. Appl. **15**, 044024 (2021).
[51] N. Muhammad, Y. Chen, C. Qiu, and G. Wang, Optical bound states in continuum in MoS_2-based metasurface for directional light emission, Nano Lett. **21**, 967 (2021).
[52] S. Romano, G. Zito, S. Torino, G. Calafiore, E. Penzo, G. Coppola, S. Cabrini, I. Rendina, and V. Mocella, Label-free sensing of ultralow-weight molecules with all dielectric metasurfaces supporting bound states in the continuum, Photonics Res. **6**, 726 (2018).
[53] Y. Zhang, W. Liu, Z. Li, Z. Li, H. Cheng, S. Chen, and J. Tian, High-quality-factor multiple fano resonances for refractive index sensing, Opt. Lett. **43**, 1842 (2018).
[54] Y. Wang, Z. Han, Y. Du, and J. Qin, Ultrasensitive terahertz sensing with high-Q toroidal dipole resonance governed by bound states in the continuum in all-dielectric metasurface, Nanophotonics **10**, 1295 (2021).
[55] S. I. Azzam, V. M. Shalaev, A. Boltasseva, and A. V. Kildishev, Formation of Bound States in the Continuum in Hybrid Plasmonic-Photonic Systems, Phys. Rev. Lett. **121**, 253901 (2018).
[56] M. Meudt, C. Bogiadzi, K. Wrobel, and P. Görrn, Hybrid photonic–plasmonic bound states in continuum for enhanced light manipulation, Adv. Opt. Mater. **8**, 2000898 (2020).
[57] L. Ni, Z. Wang, C. Peng, and Z. Li, Tunable optical bound states in the continuum beyond in-plane symmetry protection, Phys. Rev. B **94**, 245148 (2016).
[58] C. W. Hsu, B. Zhen, J. Lee, S. Chua, S. G. Johnson, J. D. Joannopoulos, and M. Soljačić, Observation of trapped light within the radiation continuum, Nature **499**, 188 (2013).
[59] M. Minkov, I. A. D. Williamson, M. Xiao, and S. Fan, Zero-Index Bound States in the Continuum, Phys. Rev. Lett. **121**, 263901 (2018).
[60] J. Jin, X. Yin, L. Ni, M. Soljačić, B. Zhen, and C. Peng, Topologically enabled ultrahigh-Q guided resonances robust to out-of-plane scattering, Nature **574**, 501 (2019).
[61] M. Kang, S. Zhang, M. Xiao, and H. Xu, Merging Bound States in the Continuum at Off-High Symmetry Points, Phys. Rev. Lett. **126**, 117402 (2021).
[62] F. Wu, J. Wu, Z. Guo, H. Jiang, Y. Sun, Y. Li, J. Ren, and H. Chen, Giant Enhancement of the Goos-Hänchen Shift Assisted by Quasibound States in the Continuum, Phys. Rev. Appl. **12**, 014028 (2019).
[63] F. Wu, M. Luo, J. Wu, C. Fan, X. Qi, Y. Jian, D. Liu, S. Xiao, G. Chen, H. Jiang, Y. Song, and H. Chen, Dual quasibound states in the continuum in compound grating waveguide structures for large positive and negative Goos-Hänchen shifts with perfect reflection, Phys. Rev. A **104**, 023518 (2021).
[64] Z. F. Sadrieva, I. S. Sinev, K. L. Koshelev, A. Samusev, I. V. Iorsh, O. Takayama, R. Malureanu, A. A. Bogdanov, and A. V. Lavrinenko, Transition from optical bound states in the continuum to leaky resonances: Role of substrate and roughness, ACS Photonics **4**, 723 (2017).
[65] D. A. Bykov, E. A. Bezus, and L. L. Doskolovich, Coupled-wave formalism for bound states in the continuum in guided-mode resonant gratings, Phys. Rev. A **99**, 063805 (2019).
[66] X. Yin, J. Jin, M. Soljačić, C. Peng, and B. Zhen, Observation of topologically enabled unidirectional guided resonances, Nature **580**, 467 (2020).
[67] B. Wu, J. Yang, P. S. Pankin, C. Huang, W. Lee, D. N. Maksimov, I. V. Timofeev, and K. Chen, Quasi-Bound states in the continuum with temperature-tunable Q factors and critical coupling point at brewster's angle, Laser Photonics Rev. **15**, 2000290 (2021).
[68] J. Bresco, D. Artigas, and L. Torner, Anistropy-induced photonic bound states in the continuum, Nat. Photonics **11**, 232 (2017).
[69] K. Koshelev, S. Lepeshov, M. Liu, A. Bogdanov, and Y. Kivshar, Metasurfaces with High-Q Resonances Governed by Bound States in the Continuum, Phys. Rev. Lett. **121**, 193903 (2018).
[70] M. Liu and D. Choi, Extreme huygens' metasurfaces based on quasi-bound states in the continuum, Nano Lett. **18**, 8062 (2018).
[71] L. Cong and R. Singh, Symmetry-Protected dual bound states in the continuum in metamaterials, Adv. Opt. Mater. **7**, 1900383 (2019).
[72] A. S. Kupriianov, Y. Xu, A. Sayanskiy, V. Dmitriev, Y. S. Kivshar, and V. R. Tuz, Metasurface Engineering Through

Bound States in the Continuum, Phys. Rev. Appl. **12**, 014024 (2019).

[73] T. C. W. Tan, E. Plum, and R. Singh, Lattice-Enhanced fano resonances from bound states in the continuum metasurfaces, Adv. Opt. Mater. **8**, 1901572 (2020).

[74] M. V. Gorkunov, A. A. Antonov, and Y. S. Kivshar, Metasurfaces with Maximum Chirality Empowered by Bound States in the Continuum, Phys. Rev. Lett. **125**, 093903 (2020).

[75] M. V. Gorkunov, A. A. Antonov, V. R. Tuz, A. S. Kupriianov, and Y. S. Kivshar, Bound states in the continuum underpin near-lossless maximum chirality in dielectric metasurfaces, Adv. Opt. Mater. **9**, 2100797 (2021).

[76] A. Overvig, N. Yu, and A. Alù, Chiral Quasi-Bound States in the Continuum, Phys. Rev. Lett. **126**, 073001 (2021).

[77] K. Kim and J. Kim, High-Q chiroptical resonances by quasi-bound states in the continuum in dielectric metasurfaces with simultaneously broken In-plane inversion and mirror symmetries, Adv. Opt. Mater. **1**, 2101162 (2021).

[78] Z. Guo, Y. Long, H. Jiang, J. Ren, and H. Chen, Anomalous unidirectional excitation of high-k hyperbolic modes using all-electric metasources, Adv. Photon. **3**, 036001 (2021).